Cooperative simultaneous inversion of satellite-based real-time PM<inf>2.5</inf> and ozone levels using an improved deep learning model

Downloaded from: https://research.chalmers.se, 2025-12-05 03:27 UTC

Citation for the original published paper (version of record):

Yan, X., Zuo, C., Li, Z. et al (2023). Cooperative simultaneous inversion of satellite-based real-time PM<inf>2.5</inf> and ozone
levels using an improved deep learning model with attention mechanism. Environmental Pollution, 327. http://dx.doi.org/10.1016/j.envpol.2023.121509

N.B. When citing this work, cite the original published paper.

research.chalmers.se offers the possibility of retrieving research publications produced at Chalmers University of Technology. It covers all kind of research output: articles, dissertations, conference papers, reports etc. since 2004. research.chalmers.se is administrated and maintained by Chalmers Library

(article starts on next page)

Environmental Pollution 327 (2023) 121509

Contents lists available at ScienceDirect

Environmental Pollution

journal homepage: www.elsevier.com/locate/envpol

Cooperative simultaneous inversion of satellite-based real-time $PM_{2.5}$ and ozone levels using an improved deep learning model with attention mechanism☆

Xing Yan [a], Chen Zuo [a], Zhanqing Li [b], Hans W. Chen [c,d,*], Yize Jiang [a], Bin He [e], Huiming Liu [f], Jiayi Chen [a], Wenzhong Shi [g]

[a] State Key Laboratory of Remote Sensing Science, College of Global Change and Earth System Science, Beijing Normal University, Beijing, 100875, China
[b] Department of Atmospheric and Oceanic Science and ESSIC, University of Maryland, College Park, MD, 20740, USA
[c] Department of Physical Geography and Ecosystem Science, Lund University, Lund, Sweden
[d] Department of Space, Earth and Environment, Chalmers University of Technology, Gothenburg, 41296, Sweden
[e] College of Global Change and Earth System Science, Beijing Normal University, Beijing, 100875, China
[f] Satellite Environment Center, Ministry of Environmental Protection, Beijing, 100094, China
[g] Department of Land Surveying and Geo-Informatics, The Hong Kong Polytechnic University, Hong Kong, China

ARTICLE INFO

Keywords:
Satellite
Real-time
$PM_{2.5}$
Ozone
Deep learning model

ABSTRACT

Ground-level fine particulate matter ($PM_{2.5}$) and ozone (O_3) are air pollutants that can pose severe health risks. Surface $PM_{2.5}$ and O_3 concentrations can be monitored from satellites, but most retrieval methods retrieve $PM_{2.5}$ or O_3 separately and disregard the shared information between the two air pollutants, for example due to common emission sources. Using surface observations across China spanning 2014–2021, we found a strong relationship between $PM_{2.5}$ and O_3 with distinct spatiotemporal characteristics. Thus, in this study, we propose a new deep learning model called the Simultaneous Ozone and $PM_{2.5}$ inversion deep neural Network (SOPiNet), which allows for daily real-time monitoring and full coverage of $PM_{2.5}$ and O_3 simultaneously at a spatial resolution of 5 km. SOPiNet employs the multi-head attention mechanism to better capture the temporal variations in $PM_{2.5}$ and O_3 based on previous days' conditions. Applying SOPiNet to MODIS data over China in 2022, using 2019–2021 to construct the network, we found that simultaneous retrievals of $PM_{2.5}$ and O_3 improved the performance compared with retrieving them independently: the temporal R^2 increased from 0.66 to 0.72 for $PM_{2.5}$, and from 0.79 to 0.82 for O_3. The results suggest that near-real time satellite-based air quality monitoring can be improved by simultaneous retrieval of different but related pollutants. The codes of SOPiNet and its user guide are freely available online at https://github.com/RegiusQuant/ESIDLM.

1. Introduction

There have been numerous occurrences of air pollution episodes with high fine particulate matter ($PM_{2.5}$) and ozone (O_3) concentration worldwide in recent decades (Zang et al., 2021a,b; Luo et al., 2022). These pollutants have adversely affected human health and can cause various diseases (Smith et al., 2009; Patella et al., 2018; Yang et al., 2022a). In China particularly, the government has prioritized $PM_{2.5}$ and O_3 synergistic control (Xiao et al., 2022). Under these issues, real-time $PM_{2.5}$ and O_3 monitoring is critical to provide immediate alerts to residents and to help governments take timely actions (Kerekes et al., 2020; Geng et al., 2021; Ojha et al., 2022).

Although ground-based measurement sites can provide real-time surface $PM_{2.5}$ and O_3 information, the availability of timely updates of $PM_{2.5}$ and O_3 levels for locations with no monitoring station is severely limited (Chae et al., 2021). To address this limitation, satellite-based technology has been widely applied for spatial coverage of $PM_{2.5}$ and O_3 estimation (Li and Cheng, 2021; Tritscher et al., 2021; Bai et al., 2022; Zhu et al., 2022). Because the levels of air pollutants vary noticeably in space and time, and are associated with complex interplay between meteorological factors, deep learning-based methods have been widely utilized for $PM_{2.5}$ and O_3 retrievals (Wang et al., 2021; Yan

☆ This paper has been recommended for acceptance by Pavlos Kassomenos.

* Corresponding author. Department of Space, Earth and Environment, Chalmers University of Technology, Gothenburg, 41296, Sweden.
E-mail address: hans.chen@chalmers.se (H.W. Chen).

https://doi.org/10.1016/j.envpol.2023.121509
Received 23 February 2023; Received in revised form 28 February 2023; Accepted 22 March 2023
Available online 24 March 2023
0269-7491/© 2023 The Authors. Published by Elsevier Ltd. This is an open access article under the CC BY license (http://creativecommons.org/licenses/by/4.0/).

et al., 2021; Zang et al., 2021a,b; Pruthi and Liu, 2022). Although deep learning-based $PM_{2.5}$ and O_3 retrievals are readily available, data obtained via historical mapping and real-time monitoring are clearly different. In historical mapping based on deep learning, the data are typically randomly sampled into three subsets (Yan et al., 2020) (training, validation, and test data), and the network is trained on samples both before and after the predicted events. However, for real-time monitoring applications the training data include only past information. Consequently, the accuracy of $PM_{2.5}$ and O_3 data in real-time monitoring is significantly lower than that in historical data mapping (Geng et al., 2021), and this limitation needs to be addressed urgently.

Currently, many developed deep learning models are designed only for individual estimation of $PM_{2.5}$ or O_3 (Li and Cheng, 2021; Yan et al., 2021; Zang et al., 2021a,b; Bai et al., 2022; Luo et al., 2022). However, $PM_{2.5}$ and O_3 have common precursors, such as volatile organic compounds (see Fig. 1a), and both pollutants can be generated through the secondary reaction process, and should thus be linked to each other (Chen et al., 2019). This suggests that the monitoring accuracy for $PM_{2.5}$ and O_3 can be enhanced by exploiting their correlation in a joint retrieval. Additionally, the amount of training samples has a noticeable effect on model performance (D.R. Liu et al., 2020). For $PM_{2.5}$ and O_3 modeling, the training data are commonly collected from surface monitoring sites. However, owing to calibration, maintenance, or data transmission issues of monitoring instruments, $PM_{2.5}$ or O_3 data can be missing for certain periods of time (Fig. 1b), and this phenomenon may be severe in specific sites (Samal et al., 2021). Gaps in training data can lead to high uncertainty in deep learning-based models (Shen et al., 2018).

$PM_{2.5}$ and O_3 have distinct temporal characteristics (Deng et al., 2022) and present $PM_{2.5}$ and O_3 concentrations can partly depend on past air pollutant levels (Li et al., 2020). However, predicting $PM_{2.5}$ and O_3 concentrations using temporal feature information in deep learning models continues to be challenging. Limited studies consider the historical temporal characteristics for $PM_{2.5}$ or O_3 modeling (Li et al., 2017; Pak et al., 2020). For this issue, a long short term memory (LSTM) network has been developed and incorporated in many deep learning models to capture the $PM_{2.5}$ or O_3 long-term dependency within a particular time range (Wen et al., 2019; Pak et al., 2020; Wu et al., 2020). Wang et al. (2021) revealed that employing LSTM to describe time-dependent effects promotes accurate estimation of $PM_{2.5}$ compared to the general random forest model. However, in $PM_{2.5}$ and O_3 time series, the effect of different past days could vary. This necessitates capturing the most important past time points and giving higher weights to them, which cannot be performed by LSTM (Abbasimehr and Paki, 2022).

To fill the research gap and overcome the aforementioned limitations, we propose a new deep learning model that simultaneously performs O_3 and $PM_{2.5}$ real-time monitoring, the Simultaneous Ozone and $PM_{2.5}$ inversion deep neural Network (SOPiNet). In contrast to general deep learning models for single $PM_{2.5}$ or O_3 estimation, SOPiNet jointly learns $PM_{2.5}$ and O_3 information and retrieves them simultaneously. We designed a two-task deep neural network framework for SOPiNet with a novel loss function, which allows the model to effectively use more training data. In addition, multi-head attention was introduced to make the network learn temporal relationships across different past days. We tested and evaluated SOPiNet for real-time $PM_{2.5}$ and O_3 monitoring in China in 2022. The evaluation demonstrates that joint learning by SOPiNet for simultaneous $PM_{2.5}$ and O_3 monitoring leads to improved general performance compared to single $PM_{2.5}$ or O_3 retrievals.

2. Materials and methods

2.1. Ground-based monitoring data

Since 2013, China has established a large number of ground-based air quality monitoring stations that can provide hourly air pollutant information. (Fig. S1a). We collected $PM_{2.5}$ and O_3 in situ observations from 2019 to 2022 at 11:00 a.m. local time synchronized with overpasses of the MODIS Terra satellite. Abnormal values were removed at each site using the method reported by Zhong et al. (2022), which considers values three standard deviations away from the moving average over 1 month as outliers.

Ground-based meteorological data were collected from the National Climatic Data Center (NCDC). As a publicly available dataset, the NCDC provides access to over four hundred ground-based monitoring stations in China (Fig. S1b). In addition, boundary layer heights were calculated from the Integrated Global Radiosonde Archive (Fig. S1c) using the Richardson method. Compared with reanalysis data which are provided with a time delay (e.g., around 5 days for ERA5 and 1 month for MERRA2), the station data can offer more timely meteorological information for real-time applications. All collected air temperature, relative humidity, wind speed, boundary layer height, and visibility data were interpolated to a 5-km grid using the Empirical Bayesian Kriging method (Krivoruchko and Gribov, 2019).

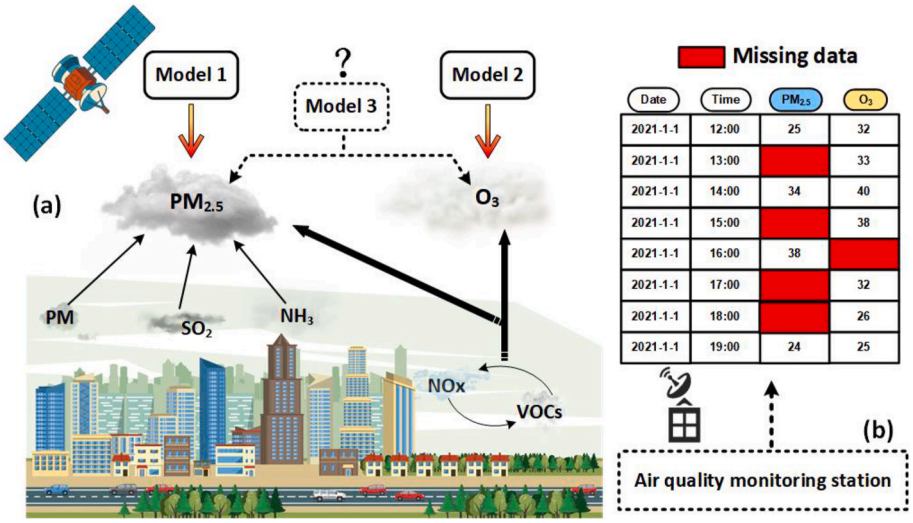

Fig. 1. (a) Schematic of potential links between particulate matter 2.5 ($PM_{2.5}$) and ozone (O_3). Model 1 and Model 2 retrieve the two air pollutant concentrations independently, while a potential Model 3 could jointly retrieve $PM_{2.5}$ and O_3. (b) Example of missing data from a hypothetical ground-based station due to sensor shutdown, system crashes, and other possible issues, which is a common problem for ground-based air quality measurements. Abbreviations: VOCs = volatile organic compounds.

2.2. MODIS data

In this study, the MODIS MOD02SSH data at a spatial resolution of 5 km were obtained from the Atmosphere Archive and Distribution System website (https://ladsweb.modaps.eosdis.nasa.gov). The MOD02SSH data product contains 36-band calibrated and geolocated at-aperture radiances, generated from MODIS Level-1A scans of raw radiance. As certain bands exhibit severe deficiencies, we used information from only band 1 to 12 and band 17 to 36 to as input for the model. Furthermore, we used MOD09, MOD13, MOD11, and MOD12 to provide surface reflectance, vegetation cover, land surface temperature, and landcover data sources for retrievals (Table S1). All these datasets were resampled to the same 5-km grid as the gridded station-based observational data.

2.3. Global forecast system data

The NASA Goddard Earth Observing System (GEOS) Composition Forecast (GEOS-CF) provides atmospheric composition data to the public in near-real time (https://gmao.gsfc.nasa.gov/). GEOS-CF along with the GEOS-Chem chemistry module expands GEOS-Chem's weather and aerosol modeling system to provide hourly atmospheric composition data including O_3 and $PM_{2.5}$ (Keller et al., 2021). In this study, we used surface-level GEOS-CF data for real-time monitoring at 11:00 (China Standard Time, CST) resampled to 5 km for the model training.

2.4. Correlation analysis between $PM_{2.5}$ and O_3

To explore the correlation between $PM_{2.5}$ and O_3, we assessed the frequency of extreme events of each day during 2014–2021 using daily averages of in-situ measurements. We used the likelihood multiplication factor (LMF) to derive the co-occurrence factor of extreme events. LMF is defined as the ratio of the joint probability of two extreme events and the probability if they are assumed to be independent, and has been widely used to assess the relationship in compound events (Zscheischler and Seneviratne, 2017). Here we defined four types of extreme events: (I) high O_3 and high $PM_{2.5}$, with O_3 and $PM_{2.5}$ both at or above their respective 80th percentile for all days; (II) high O_3 and low $PM_{2.5}$, with O_3 at or above the 80th percentile and $PM_{2.5}$ at or below the 20th percentile; (III) low O_3 and low $PM_{2.5}$, with O_3 at or below the 20th percentile and $PM_{2.5}$ at or above the 80th percentile; (IV) low O_3 and low $PM_{2.5}$, with O_3 and $PM_{2.5}$ both at or below their respective 20th percentile. The LMF formula is expressed as follows:

$$\begin{cases} I: F_{PM_{2.5},O_3}(x,y) = P\left(PM_{2.5,} \geq x, O_3 \geq y\right) \\ II: F_{PM_{2.5},O_3}(x,y) = P\left(PM_{2.5,} \leq x, O_3 \geq y\right) \\ III: F_{PM_{2.5},O_3}(x,y) = P\left(PM_{2.5,} \geq x, O_3 \leq y\right) \\ IV: F_{PM_{2.5},O_3}(x,y) = P\left(PM_{2.5,} \leq x, O_3 \leq y\right) \end{cases} \quad (1)$$

$$F_{\exp}(x,y) = (1 - x_{th})y_{th} \quad (2)$$

$$LMF = \frac{F_{PM_{2.5},O_3}(x,y)}{F_{\exp}(x,y)} \quad (3)$$

where x is the percentile in the $PM_{2.5}$ data (20th or 80th percentile) and y is the percentile in the O_3 data (20th or 80th percentile). Notably, an LMF equal to or below one represents no increase in the co-occurrence probability (i.e., the two extreme events are likely to be independent), whereas a larger LMF indicates an increased likelihood of compound events.

3. Simultaneous Ozone and $PM_{2.5}$ inversion deep neural network (SOPiNet)

We developed SOPiNet to address the following deficiencies associated with single modeling retrievals: (1) $PM_{2.5}$ and O_3 have similar emission sources and significant commonalities, and single task modeling is limited in that it cannot use shared information to improve the estimation accuracy; (2) when ground-based observations for $PM_{2.5}$ or O_3 are missing, there are gaps in the training data for single modeling; and (3) variations in the air conditions of different days in the past have different impacts on current $PM_{2.5}$ and O_3, and capturing this feature at different time points is challenging.

Fig. 2a shows the framework of SOPiNet, which consists of the following three key parts: (1) a deep neural network (DNN) to process satellite and other ancillary data; (2) multi-head attention to learn temporal relationships across different past days; and (3) joint training applied by integrating DNN and attention-based features for shared representation learning. The codes of SOPiNet and its user guide are freely available online at https://github.com/RegiusQuant/ESIDLM. All input variables for SOPiNet are shown in Table S2. The collected data from 2020 to 2021 were used as training data to train the model, the data in 2019 were used as validation data for model hyperparameter tuning, and the data in 2022 were used as test data to evaluate the model performance.

3.1. DNN framework

In SOPiNet, we introduce a DNN-based framework called Entity-DenseNet (Yan et al., 2020). The input data are separated into two groups: categorical and numerical variables. The categorical variables are first processed by an embedding layer and then merged with numerical variables as inputs to hidden layers. We constructed three hidden layers in SOPiNet, each comprising one batch normalization layer, one fully connected layer, one dropout layer, and one rectified linear unit layer. The details of the feed-forward operation in this DNN framework are reported by Yan et al. (2020).

3.2. Multi-head attention

SOPiNet learns relationships across different past days via the multi-head attention mechanism. An attention function takes as input the query (Q), keys (K), and corresponding values (V), which are all real $N \times d_{\text{model}}$ matrices (Vaswani et al., 2017):

$$Q, K, V \in R^{N \times d_{\text{model}}} \quad (4)$$

where Q, K *and* $V \in R^{N \times d_{\text{model}}}$ are Real Number (R) matrix with N and d_{model} dimensions. Then the head-specific representation subspaces Q_i, K_i, and V_i are obtained through linear projections to $N \times d_k$ and $N \times d_v$ dimensions:

$$\begin{cases} Q_i = Q \times W_i^Q, Q_i \in R^{N \times d_k} \\ K_i = K \times W_i^K, K_i \in R^{N \times d_k} \\ V_i = V \times W_i^V, V_i \in R^{N \times d_v} \end{cases} \quad (5)$$

where i denotes the head number, and W_i^Q, W_i^K, and W_i^V are head-specific weights for Q, K, and V:

$$W_i^Q \in R^{d_{\text{model}} \times d_k}, W_i^K \in R^{d_{\text{model}} \times d_k}, W_i^V \in R^{d_{\text{model}} \times d_v} \quad (6)$$

here we set $d_k = d_v = d_{\text{model}}/I$, where I is the number of heads.

A common choice for computing the attention in head_i is the scaled dot-product attention, which can be expressed as follows:

$$\text{head}_i = Attention(Q_i, K_i, V_i) = \text{softmax}\left(Q_i K_i^T \Big/ \sqrt{d_k}\right) V_i \quad (7)$$

The final multi-head attention outputs are processed by a linear combination (W^O) from all heads.

$$MultiHead(Q, K, V) = \text{concat}(head_1, head_2, \cdots head_i) W^O \quad (8)$$

where $W^O \in \mathrm{R}^{(i \cdot d_v) \times d_{\text{model}}}$. Fig. 2c shows how the multi-head attention

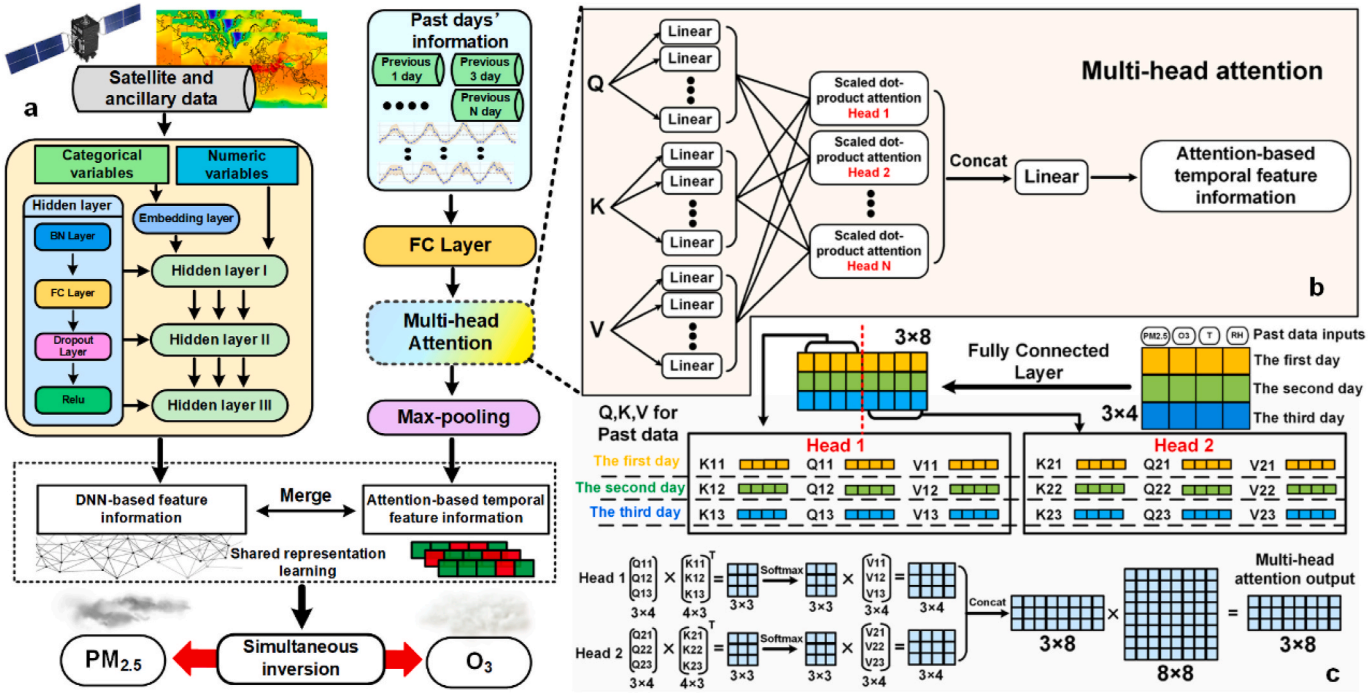

Fig. 2. (a) A schematic of the Simultaneous Ozone-$PM_{2.5}$ inversion deep neural Network (SOPiNet) framework. (b) The architecture of multi-head attention. (c) An example of how information from the past three days is used for model learning through multi-head attention. Abbreviations: BN = batch normalization, FC = fully connected, ReLU = rectified linear unit, Concat = concatenate operation.

works in this study, using information from the past 3 days as an example (in actuality we used the past 20 days). The input X (3 × 4) has 3 rows (corresponding to the number of days) and 4 columns (one for each feature: $PM_{2.5}$, O_3, temperature and relative humidity). Then, through the fully connected layer process for a linear transformation, we obtained ×2 (3 × 8). Here, the original 4 feature information is transformed to 8 dimensional feature space ($d_{model} = 8$). If the number of heads is 2, $d_k = d_v = d_{model}/I = 8/2 = 4$; therefore, Q_i, K_i, and V_i are 3 × 4 matrices. The output from head 1 and 2 are 3 × 4 matrices, and the combination of the two yields a 3 × 8 matrix. Through the linear transformation of W^O, which has 8 × 8 dimensions (i × d_v = 2 × 4 = 8, d_{model} = 8), the final output from the multi-head attention is a 3 × 8 matrix. Evidently, the input and output matrices for multi-head attention have the same dimension. This way, multi-head attention allows for the model to jointly assess information from the past days to learn their temporal relationships. In this study, we used the Autoregressive Integrated Moving Average (ARIMA) model to determine the number of past days to use as input to SOPiNet (the detailed can be found in Supplementary information- Optimization of the number of past days' information for $PM_{2.5}$ and O_3) (Sakamoto et al., 1986; Tran and Reed, 2004; Aasim et al., 2019). Based on ARIMA results, we chose to use 20 days of information as inputs for the SOPiNet real-time O_3 and $PM_{2.5}$ retrievals.

3.3. Loss function

For effective knowledge sharing across $PM_{2.5}$ and O_3 retrievals, a new joint loss function was developed for network optimization:

$$L_{total} = L_{PM_{2.5}} + L_{O_3} \tag{9}$$

with

$$\begin{cases} L_{PM_{2.5}} = \dfrac{\sum_{i=0}^{N}\left(Y_{true_i}^{PM_{2.5}} - Y_{e_i}^{PM_{2.5}} \times M_{mask_i}^{PM_{2.5}}\right)^2}{\sum_{i=0}^{N} M_{mask_i}^{PM_{2.5}}} \\ L_{O_3} = \dfrac{\sum_{i=0}^{N}\left(Y_{true_i}^{O_3} - Y_{e_i}^{O_3} \times M_{mask_i}^{O_3}\right)^2}{\sum_{i=0}^{N} M_{mask_i}^{O_3}} \end{cases} \tag{10}$$

where N is the number of samples, $Y_{true_i}^{PM_{2.5}}$ and $Y_{true_i}^{O_3}$ are ground-based measured values taken as the truth at sample i, $Y_{e_i}^{PM_{2.5}}$ and $Y_{e_i}^{O_3}$ are model estimated values, and $M_{mask_i}^{PM_{2.5}}$ and $M_{mask_i}^{O_3}$ are mask values for ground-based measured true values. If the ground-based measured value is missing, $M_{mask_i} = 0$; otherwise $M_{mask_i} = 1$.

3.4. Spatial heterogeneity and gap-filling for cloud impact

Because climate and administrative policies may differ significantly among provinces in China, $PM_{2.5}$ and O_3 have distinct spatial characteristics (Zhao et al., 2021). This study considered season, month, land use type (Table S3), and province (Table S4, Fig. S2) as categorical variables for the model to address the spatial heterogeneity issue. In addition, we used the Cartesian function to model the spatial-temporal feature interaction processes for $PM_{2.5}$ and O_3 in different locations and months:

$$S \times T = \{(s,t) | s \in S \wedge t \in T\} \tag{11}$$

where s is one of the elements for province S and t is a one of the elements for month T. We input the pairwise feature S × T to SOPiNet to jointly learn the interactions between the spatial-temporal information with O_3 and $PM_{2.5}$.

Clouds have significant impacts on satellite signals of $PM_{2.5}$ and O_3. Numerous previous studies have not performed the estimation under cloudy satellite pixels (Zang et al., 2021a,b; Li et al., 2022a; Luo et al.,

2022). To address this limitation, we first classified the satellite pixels into two types: cloud and non-cloud (Luo et al., 2008). Then SOPiNet estimated full-coverage $PM_{2.5}$ and O_3 concentrations by mining the relationship between meteorological data, GEOS-CF forecasts and ground-based $PM_{2.5}$ and O_3 under cloud and non-cloud conditions. Geng et al. (2021) showed that this method is robust and counteracted the limitations of cloudy pixels.

4. Results

4.1. Significant links between $PM_{2.5}$ and O_3

We first assessed the association between extreme $PM_{2.5}$ and O_3 events using ground-based observations from 2014 to 2021 in China. We used LMF to measure the increase in the co-occurrence probability of extreme $PM_{2.5}$ and extreme O_3 (above 80th percentile as extreme high and below 20th percentile as extreme low) compound events relative to the frequency if these extremes were independent. An LMF of 1 or below indicates no increase in the co-occurrence probability of compound extreme $PM_{2.5}$ and O_3 events. Fig. 3a–d shows that the mean LMF for four types of concurrent extreme O_3 and $PM_{2.5}$ events in four seasons during 2014–2021. The results indicate that the association between $PM_{2.5}$ and O_3 has strong seasonal and spatial characteristics. As shown in Fig. 3a and b for the winter season, the mean LMF was notably higher in northern China than in southern China, which shows the presence of both compound extreme low $PM_{2.5}$ _high O_3 and extreme high $PM_{2.5}$ _low O_3 events in northern China in winter. Many studies have presented a significant negative correlation between $PM_{2.5}$ and O_3 in winter in northern China due to temperature and emissions related to household heating (Li et al., 2019a,b; Duan et al., 2020). Li et al. (2019a,b) showed that high $PM_{2.5}$ concentrations in winter scavenge hydroperoxides (HO_2) and NO_x radicals needed to produce O_3, leading to a decrease in O_3. On the other hand, the winter season can also lead to an increase in the co-occurrence of high O_3 and low $PM_{2.5}$ in northern China. This dependence has also been observed in 12 western US cities; O_3 increased with $PM_{2.5}$ at low peaks (approximately 30–50 $\mu g/m^3$) and declined at high $PM_{2.5}$ concentration levels (Buysse et al., 2019).

In spring and autumn, the LMF for extreme high $PM_{2.5}$–low O_3 in the Beijing-Tianjin-Hebei region is generally above 2.0, but for extreme low $PM_{2.5}$–high O_3 the LMF is always below 1 (Fig. 3e), leading to a doubling in the occurrence rate for high $PM_{2.5}$ and low O_3 events. In spring, this region often suffer from dust storms, which directly affect the radiative forcing and thus the secondary production of O_3 (Forkel et al., 2012; Huang et al., 2014; Kok et al., 2021). In summer, Fig. 3c and d shows that the co-occurrence of extreme high $PM_{2.5}$– high O_3 is especially high. In this season, the enhancement of solar radiation promotes

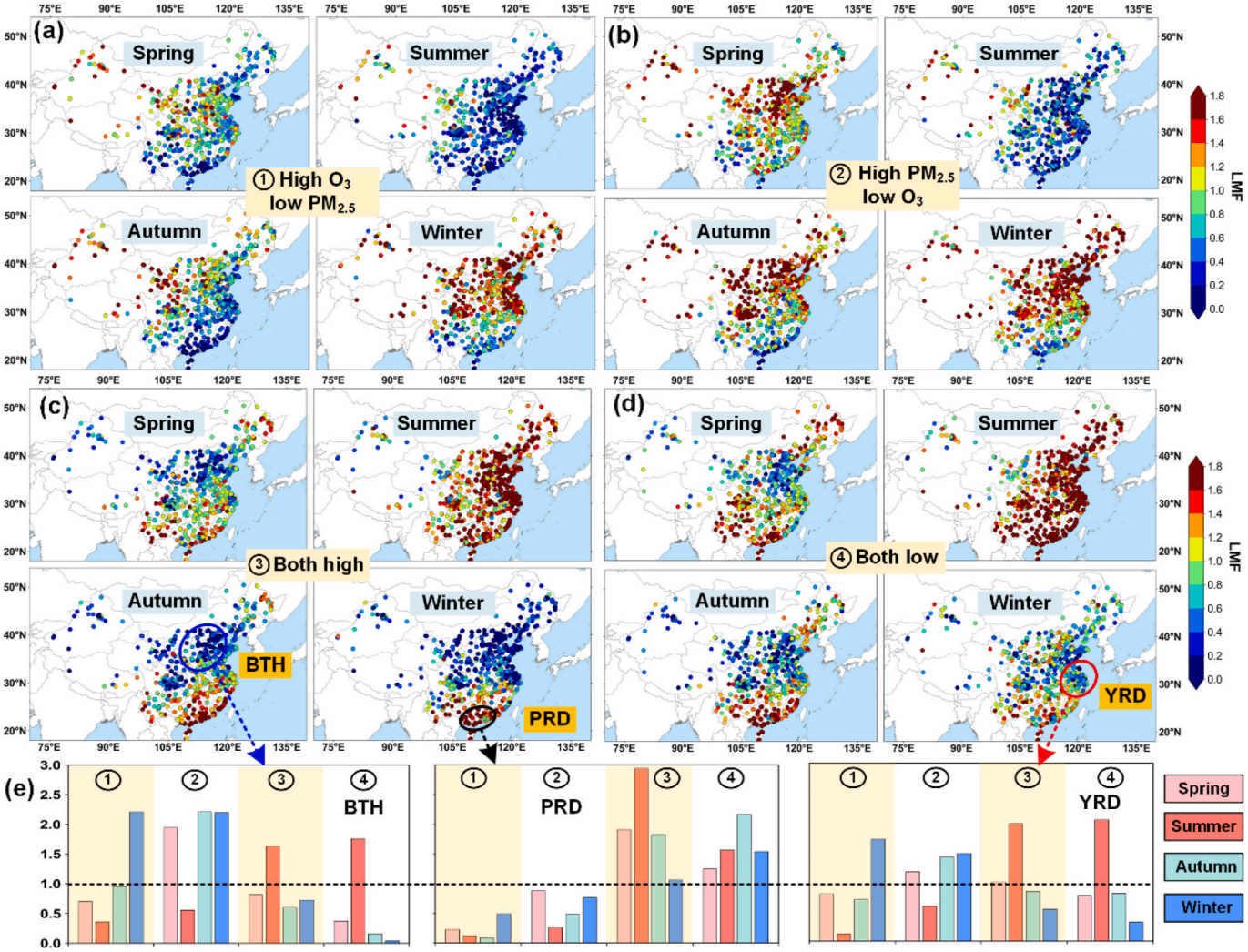

Fig. 3. (a)–(d) Mean LMF of four types of concurrent extreme O_3 and extreme $PM_{2.5}$ events in four seasons based on ground-based measurements during 2014–2021. The mean LMF in three mega-city regions: Beijing-Tianjin-Hebei (BTH; 37°–41°N, 114°–118°E), Yangtze River Delta (YRD; 30°–33°N, 118°–122°E) and Pearl River Delta (PRD; 21.5°–24°N, 112°–115.5°E). The black dotted line denotes where the LMF is 1.

photochemical reactions that lead to O_3 generation. Then, high levels of atmospheric oxidants ($O_X = NO_2 + O_3$) can lead to a low oxidation state, oxidizing organic aerosols and resulting in joint extreme high O_3 and $PM_{2.5}$ events (Duan et al., 2020). Previous studies have found that O_3 and $PM_{2.5}$ are more likely to exhibit a strong positive association in summer, especially in coastal regions such as the Pearl River Delta and Yangtze River Delta, which is consistent with our findings, as shown in Fig. 3c–e. Our analysis reveals a strong relationship between $PM_{2.5}$ and O_3, and the compound extremes of $PM_{2.5}$ and O_3 events have clear spatial and temporal patterns in China. Therefore, jointly learning $PM_{2.5}$ and O_3 information through deep learning could potentially take advantage of this relationship to improve the retrievals of $PM_{2.5}$ and O_3 in different regions and seasons.

4.2. Model evaluation and comparison

To quantify the added value of the joint learning in SOPiNet, we predicted real-time values of $PM_{2.5}$ and O_3 in 2022 using SOPiNet and compared the results with a single modeling variant of the network that retrieved $PM_{2.5}$ and O_3 independently. Fig. 4a–d shows the predicted values evaluated against observations in a time-based validation (2020–2021 as training data, 2019 as validation data and 2022 as test data). For $PM_{2.5}$, the results from SOPiNet are generally consistent with ground-based observations, with a coefficient of determination (R^2) of 72% and RMSE of 16.45 μg/m^3, thus achieving an additional 6 percentage point of variance compared to the single modeling results (R^2 = 66%).

In addition, we divided the concentrations into three intervals: 0–50, 50–100, and 100–150 μg/m^3. The result shows that SOPiNet has significantly higher R^2 than single modeling for $PM_{2.5}$ ranging from 50 to 100 μg/m^3 (SOPiNet R^2 = 72%, single modeling R^2 = 63%) and 100–150 μg/m^3 (SOPiNet R^2 = 62%, single modeling R^2 = 55%), which indicates that the joint learning especially improved the result for high $PM_{2.5}$ concentrations (exceeding 50 μg/m^3). For the O_3 validation, SOPiNet yields R^2 and RMSE values of 82% and 12.60 μg/m^3, while single modeling has an R^2 and RMSE of 79% and 13.87 μg/m^3, respectively. Based on the intervals, SOPiNet has a strong advantage over single modeling for O_3 in the 50–150 μg/m^3 range, where the joint learning led to a 3 percentage point increase in the explained variance in O_3.

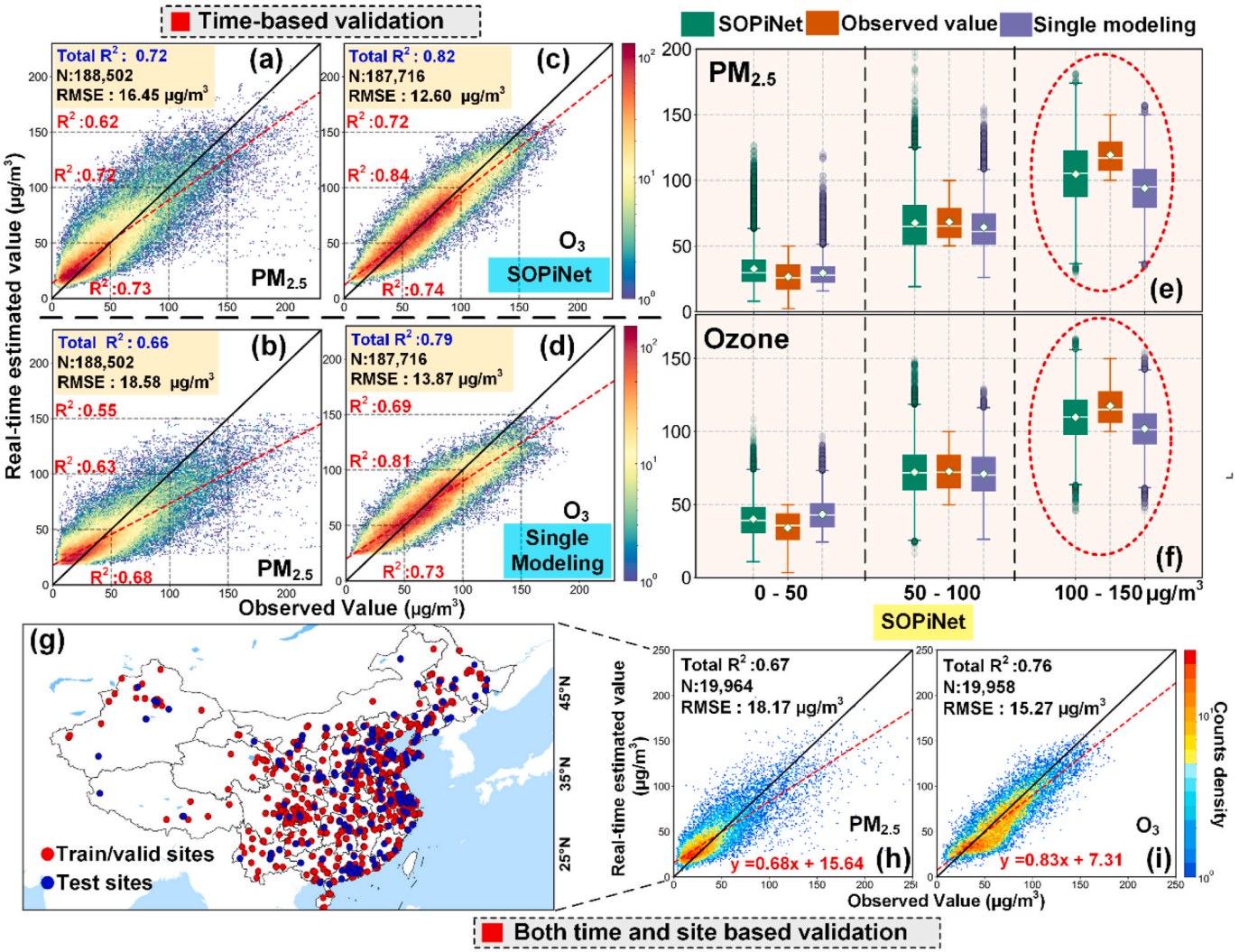

Fig. 4. (a–d) Validation of SOPiNet and single modeling against ground-based observations. The solid black line is the 1:1 reference line. The solid red line is the linear regression fitted line. The linear regression relation, coefficient of determination (R^2), number of samples (N) and root-mean-square error (RMSE) are presented in each panel, along with the R^2 and RMSE values for specific concentration intervals. (e–f) Box plots of SOPiNet estimates, single modeling estimates and in-situ measurements in three intervals (0–50 μg/m^3, 50–100 μg/m^3 and 50–150 μg/m^3). (g) The stations used to test the performance of SOPiNet in regions with no ground-based measurements. (h–i) Validation results from (g). (For interpretation of the references to colour in this figure legend, the reader is referred to the Web version of this article.)

From Fig. 4a–d, it can be seen that SOPiNet has more reliable estimates for high levels of $PM_{2.5}$ and O_3 compared with the single modeling results. In particular, SOPiNet reduces the underestimation issue in the 50–150 μg/m^3 range for both the $PM_{2.5}$ and O_3 retrievals (Fig. 4e and f). Table S5 lists the performances of models from previous studies which used the time-based method for validation (Xue et al., 2019; R.Y. Liu et al., 2020; Wei et al., 2020; Yan et al., 2020; Chen et al., 2021; Geng et al., 2021; Huang et al., 2021; Yan et al., 2021; Dong et al., 2022; Luo et al., 2022; Wang et al., 2022). From the comparison with previous studies, SOPiNet exhibits certain improvements with respect to R^2 and RMSE.

To evaluate the performance of SOPiNet in areas where there are no ground-based stations to provide training data, we randomly excluded 200 observational sites (Fig. 4g) from the training set. The validation results in Fig. 4h and i shows that SOPiNet still performs well in areas with no stations, with an R^2 of 67% for $PM_{2.5}$ and 76% for O_3.

In addition, compared with single $PM_{2.5}$ and O_3 retrievals, SOPiNet significantly reduced the training and inference time (see Table S6). SOPiNet decreased the training time by 35.5% and inference time by 32.0% on a computer with a 3960X 24-Core CPU and an NVIDIA GeForce RTX 3090 GPU.

One reason for the improved accuracy by SOPiNet is its ability to utilize more training samples than single modeling. As seen in Fig. 5a, many sites had missing data for $PM_{2.5}$ when O_3 measurements were available, and vice versa. Missing data rates exceeding 5% ($PM_{2.5}$ or O_3) were observed in 36.5% of the sites. Particularly, as shown in Fig. S4, certain sites can have missing data rates that exceed 20% with a maximum of 56.3%. Single modeling works only when there is no missing data in each estimation task (Fig. 5b), leading to many collected incomplete data not being used for model training. In contrast, SOPiNet can train a model despite either $PM_{2.5}$ or O_3 data missing, which may present additional samples for training data (used to train the model) and validation data (used for model hyperparameter tuning) compared to single modeling. Fig. 5c presents a comparison of the model performance under different data missing rates. The advantage of SOPiNet over single modeling clearly increases as the missing data rate increases. When the missing data rate exceeds 20%, SOPiNet yields increased R^2 values by 11.1% and 6.4% (relative change) for real-time $PM_{2.5}$ and O_3 estimation, and decreased RMSE values by 12.4% and 6.9% (Fig. S5), respectively.

4.3. Real-time monitoring across China in full coverage

Fig. 6 shows daily real-time monitoring results obtained by SOPiNet for three conditions: heavy, moderate, and few clouds on January 26, May 7, and 7 March 2022, respectively. On January 26, 2022, the cloud-free satellite pixels covered only 20–30% of the grid cells in China. Under this condition, many hotspots of $PM_{2.5}$ and O_3 were missing owing to the effect of clouds. SOPiNet first classifies the pixels as cloud or non-cloud, then using supportive information from GEOS-CF data ($PM_{2.5}$ and O_3) and meteorological data, conducts joint learning to explore the implicit relationship between variables from the actual $PM_{2.5}$ and O_3 states. Consequently, the weight coefficient associated with the cloud and non-cloud conditions can be learned during the SOPiNet training, which allows the model to effectively train cloud-affected areas, thereby driving other variables to fill in the gaps. From the results on January 26, 2022, SOPiNet can accurately capture the heavy $PM_{2.5}$ (>100 μg/m^3) and slightly O_3 polluted (<40 μg/m^3) condition in the Beijing-Tianjin-Hebei region, but this is not detected without gap-filling for cloud impact. These improvements were observed under moderate and few clouds conditions, during which SOPiNet can comprehensively capture daily variations in $PM_{2.5}$ and O_3.

Fig. S9a and c show a detailed comparison between SOPiNet real-time simultaneous inversion and the in-situ ground measurements. The temporal correlation coefficients (R) between the retrieved and observed concentrations are 0.91 and 0.96 for $PM_{2.5}$ and O_3, respectively. Generally, high pollution can cause large uncertainties in real-time monitoring. We calculated the accuracy of SOPiNet for real-time alerts when $PM_{2.5}$ and O_3 levels are dangerous to human health (>100 μg/m^3). As presented in Figs. S9b and d, SOPiNet yields a mean accuracy of approximately 85.2% for high level pollution days. Fig. S9e–j show two cases of comparisons between SOPiNet estimates

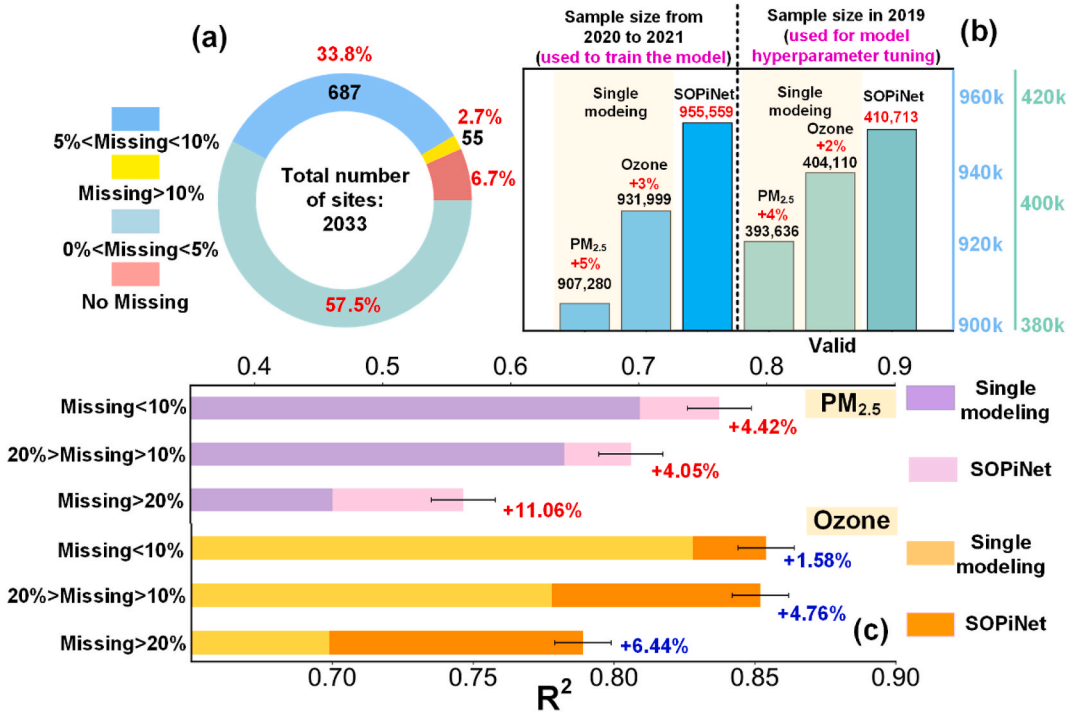

Fig. 5. (a) Percentages of missing in-situ ground measurements in China during 2019–2021. (b) Improvement of SOPiNet in data utilization over single modeling. (c) Comparison between the R^2 values of different groups with missing data based on SOPiNet and single modeling.

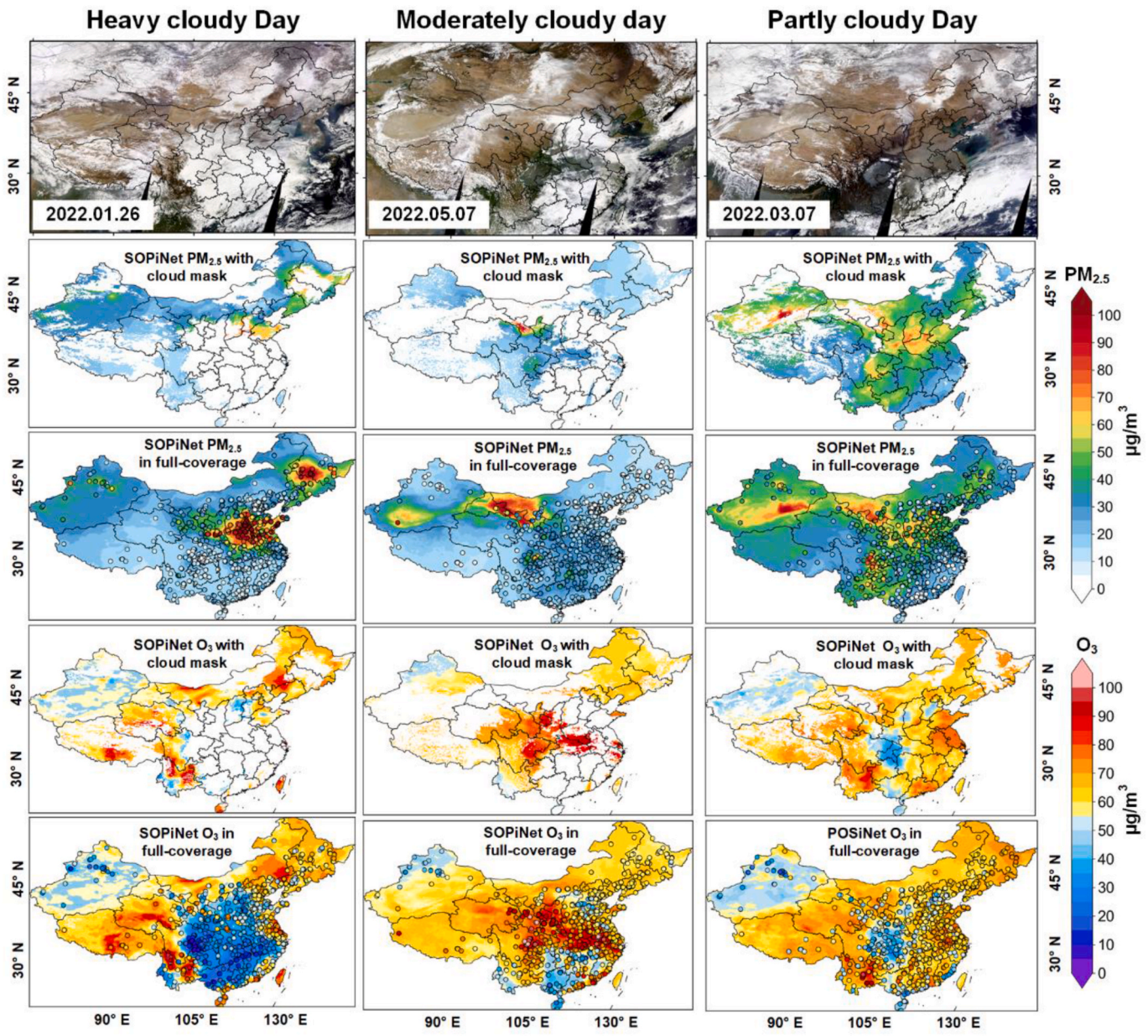

Fig. 6. Daily full coverage of $PM_{2.5}$ and O_3 concentrations based on real-time monitoring from SOPiNet with ground-based observations (third row, fifth row) compared with estimates under cloud masking (second row, forth row). Three cases with different cloud conditions (heavily, moderately, and partly cloudy) are presented.

and GEOS-CF forecasts. On January 5, 2022, high $PM_{2.5}$ pollution was clearly observed in the Yangtze River Delta and northeast China. Although both SOPiNet and GEOS-CF captured these hotspots, GEOS-CF severely overestimated the $PM_{2.5}$ concentration in Sichuan; the $PM_{2.5}$ concentrations from ground-based measurements and SOPiNet retrievals were approximately 50 $\mu g/m^3$, while the GEOS-CF $PM_{2.5}$ forecast exceeded 90 $\mu g/m^3$. On Apr 12, 2022, GEOS-CF underestimated (overestimated) O_3 in the Northeast (Southwest) region of China, while SOPiNet accurately captured these events.

5. Conclusion and discussion

This study proposes a novel satellite-based inversion deep learning model, SOPiNet, for real-time and simultaneous $PM_{2.5}$ and O_3 monitoring. First, the relation between O_3 and $PM_{2.5}$ was illustrated. The presence of both compound extreme low $PM_{2.5}$–high O_3 and extreme high $PM_{2.5}$–low O_3 events were found in northern China in winter. Additionally, the co-occurrences of both high O_3–high $PM_{2.5}$ and low O_3–low $PM_{2.5}$ were especially high in western China during summer. To better model this highly relevant relationship and improve real-time O_3 and $PM_{2.5}$ monitoring, SOPiNet was designed within a two-task deep neural network framework, which simultaneously learns $PM_{2.5}$ and O_3 retrieval tasks and shares the most relevant features of both.

Moreover, we found that historical air conditions from the past days to weeks contain information relevant for the estimation of current $PM_{2.5}$ and O_3 (Fig. S7). We determined that including information about the air quality from the past 20 days was optimal for current real-time $PM_{2.5}$ and O_3 estimation in SOPiNet. The important features from the past days were captured in SOPiNet using the multi-head attention mechanism. As shown in Fig. 4, validation results show that SOPiNet is suitable for the simultaneous inversion of $PM_{2.5}$ and O_3, and results in an overall performance compared to the single-species inversion model. One reason for this improvement is that SOPiNet utilizes more samples in the training dataset when data is missing for one species but available

for the other species; consequently, the joint retrieval is particularly beneficial in cases where missing data rates are high.

A limitation of SOPiNet that should be addressed in future studies is that the model cannot be trained when $PM_{2.5}$ and O_3 exhibit missing data simultaneously. Many existing research studies indicate that missing training samples have significant impacts on model performance (Shen et al., 2018; Samal et al., 2021; Yang et al., 2022b; Li et al., 2022b). Therefore, comprehensive utilization of the collected data is challenging, and further investigation is needed to handle missing data. On the other hand, SOPiNet employs multi-head attention to capture patterns existing in time series, but the mechanism for visualizing this pattern has not been determined. Moreover, the same meteorological factors in different weather conditions could have different impacts on the $PM_{2.5}$ and O_3 retrieval. Although the potential dependence of the shared meteorological factors on different impacts can be captured by SOPiNet with shared representation learning, it is currently challenging to physically interpret the results. Therefore, further work is needed to open the deep learning black box to understand the processes that improve the prediction of air pollution.

Author statement

Xing Yan: Conceptualization, Methodology, Investigation, Writing - Original Draft. **Chen Zuo**: Writing - Original Draft, Validation, Formal analysis, Data Curation. **Zhanqing Li**: Writing - Review & Editing, Project administration. **Hans W. Chen**: Writing - Original Draft, Writing - Review & Editing, Investigation. **Yize Jiang**: Methodology, Software. **Bin He**: Writing - Review & Editing. **Huiming Liu**: Writing - Review & Editing. **Jiayi Chen**: Data Curation. **Wenzhong Shi**: Writing - Review & Editing.

Declaration of competing interest

The authors declare that they have no known competing financial interests or personal relationships that could have appeared to influence the work reported in this paper.

Data availability

Data will be made available on request. The codes of SOPiNet and its user guide are freely available online at https://github.com/RegiusQuant/ESIDLM.

Acknowledgments

This research has been supported by the Natural Science Foundation of Beijing (grant no. 8222058), the National Natural Science Foundation of China (grant no. 42030606 and 42230601), the National Key Research and Development Plan of China (grant no. 2017YFC1501702), and the Fundamental Research Funds for the Central Universities.

Appendix A. Supplementary data

Supplementary data to this article can be found online at https://doi.org/10.1016/j.envpol.2023.121509.

References

Aasim, Singh, S.N., Mohapatra, A., 2019. Repeated wavelet transform based ARIMA model for very short-term wind speed forecasting. Renew. Energy 136, 758–768.
Abbasimehr, H., Paki, R., 2022. Improving time series forecasting using LSTM and attention models. J. Ambient Intell. Hum. Comput. 13, 673–691.
Bai, K.X., Li, K., Ma, M.L., Li, K.T., Li, Z.Q., Guo, J.P., Chang, N.B., Tan, Z., Han, D., 2022. LGHAP: the Long-term gap-free high-resolution air pollutant concentration dataset, derived via tensor-flow-based multimodal data fusion. Earth Syst. Sci. Data 14, 907–927.
Buysse, C.E., Kaulfus, A., Nair, U., Jaffe, D.A., 2019. Relationships between particulate matter, ozone, and nitrogen oxides during urban smoke events in the western US. Environ. Sci. Technol. 53, 12519–12528.
Chae, S., Shin, J., Kwon, S., Lee, S., Kang, S., Lee, D., 2021. PM10 and PM2.5 real-time prediction models using an interpolated convolutional neural network. Sci. Rep. 11.
Chen, J.J., Shen, H.F., Li, T.W., Peng, X.L., Cheng, H.R., Ma, C.Y., 2019. Temporal and spatial features of the correlation between PM2.5 and O-3 concentrations in China. Int. J. Environ. Res. Publ. Health 16.
Chen, L., Liang, S., Li, X.L., Mao, J., Gao, S., Zhang, H., Sun, Y.L., Vedal, S., Bai, Z.P., Ma, Z.X., Haiyu, Azzi, M., 2021. A hybrid approach to estimating long-term and short-term exposure levels of ozone at the national scale in china using land use regression and bayesian maximum entropy. Sci. Total Environ. 752.
Deng, C.X., Tian, S., Li, Z.W., Li, K., 2022. Spatiotemporal characteristics of PM2.5 and ozone concentrations in Chinese urban clusters. Chemosphere 295.
Dong, L.C., Li, S.W., Xing, J., Lin, H., Wang, S.S., Zeng, X.Y., Qin, Y.M., 2022. Joint features random forest (JFRF) model for mapping hourly surface PM2.5 over China. Atmos. Environ. 273.
Duan, J., Huang, R.J., Li, Y.J., Chen, Q., Zheng, Y., Chen, Y., Lin, C.S., Ni, H.Y., Wang, M., Ovadnevaite, J., Ceburnis, D., Chen, C.Y., Worsnop, D.R., Hoffmann, T., O'Dowd, C., Cao, J.J., 2020. Summertime and wintertime atmospheric processes of secondary aerosol in Beijing. Atmos. Chem. Phys. 20, 3793–3807.
Forkel, R., Werhahn, J., Hansen, A.B., McKeen, S., Peckham, S., Grell, G., Suppan, P., 2012. Effect of aerosol-radiation feedback on regional air quality - a case study with WRF/Chem. Atmos. Environ. 53, 202–211.
Geng, G.N., Xiao, Q.Y., Liu, S.G., Liu, X.D., Cheng, J., Zheng, Y.X., Xue, T., Tong, D., Zheng, B., Peng, Y.R., Huang, X.M., He, K.B., Zhang, Q., 2021. Tracking air pollution in China: near real-time PM2.5 retrievals from multisource data fusion. Environ. Sci. Technol. 55, 12106–12115.
Huang, C.H., Hu, J.L., Xue, T., Xu, H., Wang, M., 2021. High-resolution spatiotemporal modeling for ambient PM2.5 exposure assessment in China from 2013 to 2019. Environ. Sci. Technol. 55, 2152–2162.
Huang, R.J., Zhang, Y.L., Bozzetti, C., Ho, K.F., Cao, J.J., Han, Y.M., Daellenbach, K.R., Slowik, J.G., Platt, S.M., Canonaco, F., Zotter, P., Wolf, R., Pieber, S.M., Bruns, E.A., Crippa, M., Ciarelli, G., Piazzalunga, A., Schwikowski, M., Abbaszade, G., Schnelle-Kreis, J., Zimmermann, R., An, Z.S., Szidat, S., Baltensperger, U., El Haddad, I., Prevot, A., 2014. High secondary aerosol contribution to particulate pollution during haze events in China. Nature 514, 218–222.
Keller, C.A., Knowland, K.E., Duncan, B.N., Liu, J.H., Anderson, D.C., Das, S., Lucchesi, R. A., Lundgren, E.W., Nicely, J.M., Nielsen, E., Ott, L.E., Saunders, E., Strode, S.A., Wales, P.A., Jacob, D.J., Pawson, S., 2021. Description of the NASA GEOS composition forecast modeling system GEOS-CF v1.0. J. Adv. Model. Earth Syst. 13.
Kerekes, J.P., Patel, M.M., D'Angelo, C.C., 2020. Review of Global Near Real Time PM2.5 Estimates and Model Forecasts.
Kok, J.F., Adebiyi, A.A., Albani, S., Balkanski, Y., Checa-Garcia, R., Chin, M.A., Colarco, P.R., Hamilton, D.S., Huang, Y., Ito, A., Klose, M., Li, L.L., Mahowald, N.M., Miller, R.L., Obiso, V., Garcia-Pando, C.P., Rocha-Lima, A., Wan, J.S., 2021. Contribution of the world's main dust source regions to the global cycle of desert dust. Atmos. Chem. Phys. 21, 8169–8193.
Krivoruchko, K., Gribov, A., 2019. Evaluation of empirical Bayesian kriging. Spatial Statistics 32.
Li, K., Jacob, D.J., Liao, H., Shen, L., Zhang, Q., Bates, K.H., 2019a. Anthropogenic drivers of 2013–2017 trends in summer surface ozone in China. Proc. Natl. Acad. Sci. - PNAS 116, 422–427.
Li, K., Jacob, D.J., Liao, H., Zhu, J., Shah, V., Shen, L., Bates, K.H., Zhang, Q., Zhai, S.X., 2019b. A two-pollutant strategy for improving ozone and particulate air quality in China. Nat. Geosci. 12, 906.
Li, T.W., Cheng, X., 2021. Estimating daily full-coverage surface ozone concentration using satellite observations and a spatiotemporally embedded deep learning approach. Int. J. Appl. Earth Obs. Geoinf. 101.
Li, T.Y., Hua, M., Wu, X., 2020. A hybrid CNN-LSTM model for forecasting particulate matter (PM2.5). IEEE Access 8, 26933–26940.
Li, X., Peng, L., Yao, X.J., Cui, S.L., Hu, Y., You, C.Z., Chi, T.H., 2017. Long short-term memory neural network for air pollutant concentration predictions: method development and evaluation. Environ. Pollut. 231, 997–1004.
Li, M.Y., Yang, Q.Q., Yuan, Q.Q., Zhu, L.Y., 2022a. Estimation of high spatial resolution ground-level ozone concentrations based on Landsat 8 TIR bands with deep forest model. Chemosphere 301.
Li, X., Zhou, Y., Wang, F., 2022b. Advanced information mining from ocean remote sensing imagery with deep learning. J. Rem. Sens. 9849645.
Liu, D.R., Lee, S.J., Huang, Y., Chiu, C.J., 2020. Air pollution forecasting based on attention-based LSTM neural network and ensemble learning. Expet Syst. 37.
Liu, R.Y., Ma, Z.W., Liu, Y., Shao, Y.C., Zhao, W., Bi, J., 2020. Spatiotemporal distributions of surface ozone levels in China from 2005 to 2017: A machine learning approach. Environ. Int. 142.
Luo, N., Zang, Z., Yin, C., Liu, M., Jiang, Y., Zuo, C., Zhao, W., Shi, W., Yan, X., 2022. Explainable and spatial dependence deep learning model for satellite-based O3 monitoring in China. Atmos. Environ. 290, 119370.
Luo, Y., Trishchenko, A.P., Khlopenkov, K.V., 2008. Developing clear-sky, cloud and cloud shadow mask for producing clear-sky composites at 250-meter spatial resolution for the seven MODIS land bands over Canada and North America. Rem. Sens. Environ. 112, 4167–4185.
Ojha, N., Soni, M., Kumar, M., Gunthe, S.S., Chen, Y., Ansari, T.U., 2022. Mechanisms and pathways for coordinated control of fine particulate matter and ozone. Curr. Pollut. Rep. 8, 594–604.

Pak, U., Ma, J., Ryu, U., Ryom, K., Juhyok, U., Pak, K., Pak, C., 2020. Deep learning-based PM2.5 prediction considering the spatiotemporal correlations: A case study of Beijing, China. Sci. Total Environ. 699.
Patella, V., Florio, G., Magliacane, D., Giuliano, A., Crivellaro, M.A., Di Bartolomeo, D., Genovese, A., Palmieri, M., Postiglione, A., Ridolo, E., Scaletti, C., Ventura, M.T., Zollo, A., 2018. Urban air pollution and climate change: "The Decalogue: allergy Safe Tree" for allergic and respiratory diseases care. Clin. Mol. Allergy 16, 20.
Pruthi, D., Liu, Y., 2022. Low-cost Nature-Inspired Deep Learning System for PM2.5 Forecast over Delhi, India. Environ. Int. 166.
Sakamoto, Y., Ishiguro, M., Kitagawa, G., 1986. Akaike Information Criterion Statistics. KTK Scientific Publishers, Tokyo; Hingham, MA; Dordrecht; Boston.
Samal, K., Babu, K.S., Das, S.K., 2021. Multi-directional temporal convolutional artificial neural network for PM2.5 forecasting with missing values: a deep learning approach. Urban Clim. 36.
Shen, H.F., Li, T.W., Yuan, Q.Q., Zhang, L.P., 2018. Estimating regional ground-level PM2.5 directly from satellite top-of-atmosphere reflectance using deep belief networks. J. Geophys. Res. Atmos. 123, 13875–13886.
Smith, K.R., Jerrett, M., Anderson, H.R., Burnett, R.T., Stone, V., Derwent, R., Atkinson, R.W., Cohen, A., Shonkoff, S.B., Krewski, D., Pope, C.A., Thun, M.J., Thurston, G., 2009. Health and Climate Change 5 Public health benefits of strategies to reduce greenhouse-gas emissions: health implications of short-lived greenhouse pollutants. Lancet (N. Am. Ed.) 374, 2091–2103.
Tran, N., Reed, D.A., 2004. Automatic ARIMA time series modeling for adaptive I/O prefetching. IEEE Trans. Parallel Distr. Syst. 15, 362–377.
Tritscher, I., Pitts, M.C., Poole, L.R., Alexander, S.P., Cairo, F., Chipperfield, M.P., Grooss, J.U., Hopfner, M., Lambert, A., Luo, B., Molleker, S., Orr, A., Salawitch, R., Snels, M., Spang, R., Woiwode, W., Peter, T., 2021. Polar stratospheric clouds: satellite observations, processes, and role in ozone depletion. Rev. Geophys. 59.
Vaswani, A., Shazeer, N., Parmar, N., Uszkoreit, J., Jones, L., Gomez, A.N., Kaiser, L., Polosukhin, I., 2017. Attention Is All You Need.
Wang, Y., Yuan, Q.Q., Li, T.W., Tan, S.Y., Zhang, L.P., 2021. Full-coverage spatiotemporal mapping of ambient PM2.5 and PM10 over China from sentinel-5P and assimilated datasets: Considering the precursors and chemical compositions. Sci. Total Environ. 793.
Wang, Y., Yuan, Q.Q., Zhu, L.Y., Zhang, L.P., 2022. Spatiotemporal estimation of hourly 2-km ground-level ozone over China based on Himawari-8 using a self-adaptive geospatially local model. Geosci. Front. 13.
Wei, J., Li, Z.Q., Cribb, M., Huang, W., Xue, W.H., Sun, L., Guo, J.P., Peng, Y.R., Li, J., Lyapustin, A., Liu, L., Wu, H., Song, Y.M., 2020. Improved 1 km resolution PM2.5 estimates across China using enhanced space-time extremely randomized trees. Atmos. Chem. Phys. 20, 3273–3289.
Wen, C.C., Liu, S., Yao, X.J., Peng, L., Li, X., Hu, Y., Chi, T.H., 2019. A novel spatiotemporal convolutional long short-term neural network for air pollution prediction. Sci. Total Environ. 654, 1091–1099.
Wu, X.L., Wang, Y., He, S.Y., Wu, Z.F., 2020. PM2.5/PM10 ratio prediction based on a long short-term memory neural network in Wuhan, China. Geosci. Model Dev. (GMD) 13, 1499–1511.
Xiao, Q.Y., Geng, G.N., Xue, T., Liu, S.G., Cai, C.L., He, K.B., Zhang, Q., 2022. Tracking PM2.5 and O-3 pollution and the related health burden in China 2013-2020. Environ. Sci. Technol. 56, 6922–6932.
Xue, T., Zheng, Y.X., Tong, D., Zheng, B., Li, X., Zhu, T., Zhang, Q., 2019. Spatiotemporal continuous estimates of PM2.5 concentrations in China, 2000-2016: a machine learning method with inputs from satellites, chemical transport model, and ground observations. Environ. Int. 123, 345–357.
Yan, X., Zang, Z., Jiang, Y.Z., Shi, W.Z., Guo, Y.S., Li, D., Zhao, C.F., Husi, L.T., 2021. A Spatial-temporal interpretable deep learning model for improving interpretability and predictive accuracy of satellite-based PM2.5. Environ. Pollut. 273.
Yan, X., Zang, Z., Luo, N.N., Jiang, Y.Z., Li, Z.Q., 2020. New interpretable deep learning model to monitor real-time PM2.5 concentrations from satellite data. Environ. Int. 144.
Yang, X.C., Wang, Y., Zhao, C.F., Fan, H., Yang, Y.K., Chi, Y.L., Shen, L.X., Yan, X., 2022a. Health risk and disease burden attributable to long-term global fine-mode particles. Chemosphere 287.
Yang, H., Wang, Q., Zhao, W., Tong, X., Atkinson, P.M., 2022b. Reconstruction of a Global 9 km, 8-Day SMAP Surface Soil Moisture Dataset during 2015–2020 by Spatiotemporal Fusion. J. Rem. Sens. 9871246, 9871246.
Zang, Z., Guo, Y.S., Jiang, Y.Z., Zuo, C., Li, D., Shi, W.Z., Yan, X., 2021a. Tree-based ensemble deep learning model for spatiotemporal surface ozone (O-3) prediction and interpretation. Int. J. Appl. Earth Obs. Geoinf. 103.
Zang, Z., Li, D., Guo, Y.S., Shi, W.Z., Yan, X., 2021b. Superior PM2.5 estimation by integrating aerosol fine mode data from the himawari-8 satellite in deep and classical machine learning models. Rem. Sens. 13.
Zhao, H., Chen, K.Y., Liu, Z., Zhang, Y.X., Shao, T., Zhang, H.L., 2021. Coordinated control of PM2.5 and O-3 is urgently needed in China after implementation of the "Air pollution prevention and control action plan". Chemosphere 270.
Zhong, J.T., Zhang, X.Y., Gui, K., Liao, J., Fei, Y., Jiang, L.P., Guo, L.F., Liu, L.K., Che, H. Z., Wang, Y.Q., Wang, D.Y., Zhou, Z.J., 2022. Reconstructing 6-hourly PM2.5 datasets from 1960 to 2020 in China. Earth Syst. Sci. Data 14, 3197–3211.
Zhu, S.Y., Xu, J., Yu, C., Wang, Y.P., Zeng, Q.L., Wang, H.M., Shi, J.C., 2022. Learning surface ozone from satellite columns (LESO): a regional daily estimation framework for surface ozone monitoring in China. IEEE Trans. Geosci. Rem. Sens. 60.
Zscheischler, J., Seneviratne, S.I., 2017. Dependence of drivers affects risks associated with compound events. Sci. Adv. 3.